JOURNAL OF THERMOPHYSICS AND HEAT TRANSFER
Vol. 17, No. 4, October–December 2003

Similarity Solution for Peritectic Solidification with Shrinkage-Induced Flow

Jae Dong Chung*
Sejong University, Seoul 143-747, Republic of Korea
and
Hoseon Yoo†
Soongsil University, Seoul 156-743, Republic of Korea

This paper deals with a similarity solution for the directional solidification of binary peritectic alloys in the presence of shrinkage-induced flow. The present model encompasses the essential ingredients of alloy solidification, such as temperature-solute coupling, macrosegregation, solid–liquid property difference, and finite back diffusion in the primary phase. A new algorithm for simultaneously determining the peritectic reaction and liquidus positions is developed, which proves to be more efficient and stable than the existing schemes. Sample calculations are performed for both hypo- and hyperperitectic compositions of a typical peritectic alloy. The results show that the present analysis is capable of properly resolving the solidification characteristics of peritectic alloys and that it can be used for validating numerical models as a test solution.

Nomenclature

C	=	solute concentration
c	=	specific heat
g	=	liquid mass fraction
h	=	enthalpy
h_f	=	latent heat of fusion
k	=	thermal conductivity
m	=	slope of the liquidus line
T	=	temperature
T_f	=	fusion temperature of the pure solvent
t	=	time
U	=	nondimensional velocity, $u/(\alpha_l/t)^{1/2}$
u	=	velocity
x	=	coordinate
α	=	thermal diffusivity, α-phase solid
β	=	microsegregation parameter, β-phase solid
δ	=	position of the phase interface
η	=	similarity variable, $x/(4\alpha_l t)^{1/2}$
κ	=	equilibrium partition coefficient
λ	=	transformed interface position, $\delta/(4\alpha_l t)^{1/2}$
ρ	=	density
ϕ	=	variable
ω	=	underrelaxation factor

Subscripts

E	=	eutectic
i	=	microscopic phase interface
L	=	liquidus
l	=	liquid
m	=	mush
P	=	peritectic
S	=	solidus
s	=	solid
W	=	wall
0	=	initial condition

Superscripts

j	=	representative of $\alpha-$ or $\beta-$ phase solid
$L-$, $L+$	=	left and right sides of liquidus
n	=	new value
$P-$, $P+$	=	left and right sides of peritectic line
α, β	=	$\alpha-$, $\beta-$ phase solid
$\hat{}$	=	ratio of the solid-to-liquid property

Received 12 November 2002; accepted for publication 4 April 2003. Copyright © 2003 by the American Institute of Aeronautics and Astronautics, Inc. All rights reserved. Copies of this paper may be made for personal or internal use, on condition that the copier pay the $10.00 per-copy fee to the Copyright Clearance Center, Inc., 222 Rosewood Drive, Danvers, MA 01923; include the code 0887-8722/03 $10.00 in correspondence with the CCC.

*Assistant Professor, Department of Mechanical Engineering; jdchung@sejong.ac.kr.

†Professor, Department of Mechanical Engineering; hsyoo@engineer.ssu.ac.kr.

I. Introduction

ANALYSIS of alloy solidification processes has attracted considerable research attention in the heat- and mass-transfer area. The trends of that research are well documented in recently published review articles. One of them[1] points out that there are three main subjects in the future direction of solidification research: rigorous analytical model, accurate simulation method, and refined experimental technique. Numerical methods, among them, have shown a certain degree of success in qualitatively predicting the macroscopic features of alloy solidification,[2,3] and encouraged by that, considerable modeling efforts have also been made to incorporate the microscopic characteristics into analyses.[4,5] In the pursuit of such model developments, one of the major problems is lack of appropriate benchmarks for quantitative assessment of proposed numerical models. An analytical solution can meet the need if it retains basic features of the solidification process under consideration. Unfortunately, most of the existing analytical or semi-analytical approaches suffer from shortcomings associated with excessive simplification in their derivation or deviation from the actual phenomena.[6–9] As an effort to establish a test solution for validation of numerical models, the present study aims to extend the previous analytical works[9–11] for eutectic alloys to peritectic systems.

Peritectic solidification involves one solid phase reacting with the liquid phase on cooling to produce a second solid phase, that is, $\alpha + L \rightarrow \beta$ (Ref. 12). Such a reaction has so far been utilized mainly for grain refinement in some Al-based alloys,[13] liquid route processing of YBCO superconductors,[14,15] and development of magnetic materials.[16] Although peritectic solidification is commonly observed in diverse alloy systems such as Zn-Cu, Zn-Ag, Ti-Al, Pb-Bi, Sn-Sb, and Ni-Al, a comprehensive understanding is still lacking.

In peritectic systems a wide spectrum of complex microstructures is found under the directional solidification conditions. Even in a

simplified case where the large temperature gradient vs growth rate ratio G/V is applied to suppress the morphological instability and ensure the planar growth of each phase, a variety of microstructures has been identified. They depend sensitively upon the relative importance of nucleation, diffusion, and convection.[17,18] Typical microstructures can be grouped into layered and nonlayered patterns. The layered structure, in which alternate bands of two solid phases develop perpendicularly to the overall growth direction, has been found in many peritectic systems: Sn-Cd (Ref. 19), Sn-Sb, Zn-Cu (Ref. 20), and Pb-Bi (Ref. 18), to name but a few. The nonlayered structure, in which initially the primary α phase forms and then transforms to the secondary β phase, has also been observed in the Pb-Bi system. Recently, Ma et al.[21] ascertained that there exists a critical composition separating the peritectic plateau into two regions where the coupled and banded growth regimes dominate, respectively. In the present study our interest is confined to the binary peritectic reaction that has the nonlayered structure.

The goals of this work are twofold: 1) to extend the previous analytical works for binary eutectic alloys to binary hyperperitectic systems, while incorporating all of the essential ingredients of alloy solidification, such as temperature-solute coupling, macrosegregation, solid–liquid property difference, and finite back diffusion in the primary solid phase; and 2) to develop a new algorithm for simultaneously determining the interface (e.g., peritectic, liquidus, and solidus) positions. The result is expected to serve as a test solution in validating sophisticated numerical models for the multicomponent alloy solidification that accompanies complicated phase equilibria.

II. Analysis

A. Modeling

Peritectic reaction concerned here, that is, $\alpha + L \rightarrow \beta$, occurs at the peritectic temperature T_P, as shown in the phase equilibrium diagram of a fictitious binary peritectic alloy (Fig. 1). The solid phase α formed at a higher temperature is termed the primary phase, and β generated at a lower temperature the secondary phase. The compositions of liquid, primary, and secondary phases at the peritectic equilibrium correspond to the points c, a, and b in Fig. 1, respectively. An alloy with the initial solute concentration higher than C_P should form the secondary solid phase β directly from the liquid. Hypoperitectic alloy has a composition between C_a and C_b, whereas hyperperitectic alloy is laid inside the compositional range from C_b to C_c. The former shows a similar solidification behavior with binary eutectic alloys, which will be addressed later. On the other hand, the latter exposes some distinguished features from the modeling of eutectic solidification: 1) four distinct regions, that is, liquid L, primary solidification $L + \alpha$, secondary solidification $L + \beta$, and solid S regions, are present in the domain; and 2) a finite jump in the liquid fraction occurs across peritectic reaction, necessitating to model discontinuous conditions at the interface between the primary and secondary solidification regions.

The physical system considered in this work is a one-dimensional directional solidification of binary peritectic alloy, as depicted schematically in Fig. 2. At $t = 0$ the alloy, which was initially at a uniform concentration C_0 and at a superheated temperature T_0, begins to solidify in a semi-infinite domain from the isothermally cooled wall. The wall temperature T_W is lower than the peritectic temperature of the alloy, so that peritectic reaction takes place. As the solidification proceeds, four distinct regions, that is, β phase solid, mush composed of liquid and β phase solid, mush composed of liquid and α phase solid, and liquid, which are bounded by the solidus, peritectic line and liquidus, respectively, appear in the system.

To render the problem analytically tractable, the following assumptions have been introduced:

1) Growth with the planar interface is assumed.

2) Undercooling is ignored so that the solidification has a single primary-to-peritectic phase transition. That is, the α phase forms from the liquid, and then transforms to the β phase in the rest of the sample.

3) Thermodynamic equilibrium holds at the microscopic solid–liquid interface, that is, $C_{si}^j = \kappa^j C_l$, where κ^j is the equilibrium partition coefficient for $j\,(=\alpha$ or $\beta)$ phase solids.

4) The liquidus line is linear, as shown in Fig. 1.

5) The macroscopic solute diffusion is negligible.

6) Flow is induced only by the solid–liquid density difference.

7) All properties are constant within individual phases, but might differ between the solid and liquid phases. The mixture volumetric properties in the mushy region, where two phases coexist, are weighted by the liquid fraction as[7,8]

$$\phi_m = (1 - g)\phi_s + g\phi_l \tag{1}$$

8) Back diffusion in the dendritic α phase solid is modeled after the Clyne and Kurz[22] microsegregation model that ensures the solute conservation.

9) Peritectic transformation occurs via equilibrium reaction. For consistency the secondary solidification obeys the lever rule. According to John and Hogan,[23] many alloys show complete

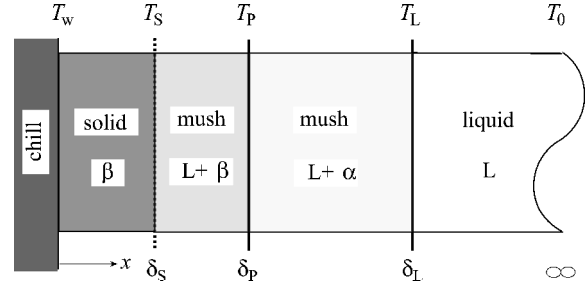

Fig. 2 Schematic of the present directional casting system.

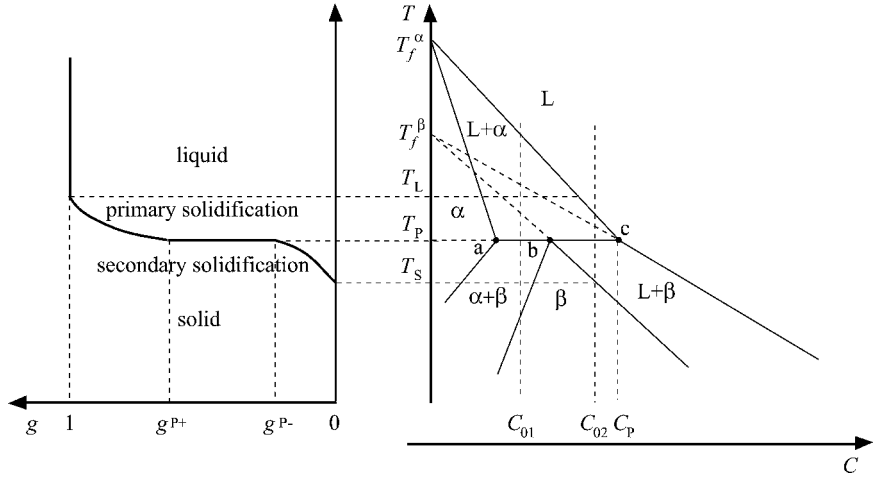

Fig. 1 Solidification of a binary peritectic alloy a) liquid fraction field and b) phase equilibrium diagram.

transformation depending on their phase diagrams. Das et al.[24] ascertained that the kinetics of primary solidification has little influence on that of peritectic transformation, supporting the introduction of this assumption independently of assumption 8. Because the rate of peritectic transformation still remains open to question, the assumption of equilibrium reaction would be the first step toward obtaining rudimentary understanding on the peritectic solidification. In the actual process the solute diffusion in the β-phase solid essentially controls both the peritectic reaction and secondary solidification.[1]

Based on the foregoing assumptions, the governing equations are derived for three distinct regions, that is, the liquid region ($\delta_L < x < \infty$), the primary solidification region ($\delta_P < x < \delta_L$), and the combined region of the secondary solidification ($\delta_S < x < \delta_P$) and solid ($0 < x < \delta_S$). The secondary solidification and solid regions are treated as a single zone (hereafter called simply the combined region). This is not only because the governing equations in the secondary solidification region include those in the solid region as a subset (when $g = 0$), but also because the interface between the two regions, that is, $x = \delta_S$, is easily identified by examining the liquid fraction field.

In the liquid region the concentration is kept constant, and the energy equation in the presence of shrinkage-induced bulk flow can easily be written as

$$\frac{\partial T}{\partial t} + u_l \frac{\partial T}{\partial x} = \alpha_l \frac{\partial^2 T}{\partial x^2} \tag{2}$$

where the bulk flow velocity is defined as $u_l = u(\delta_L)$. In both of the primary solidification and combined regions, the governing continuity, energy, and concentration equations can be cast in the same forms as

$$(1 - \hat{\rho}) \frac{\partial g}{\partial t} + \frac{\partial u}{\partial x} = 0 \tag{3}$$

$$[(1 - g)\hat{\rho}\hat{c} + g] \frac{\partial T}{\partial t} + u \frac{\partial T}{\partial x} + \left[\hat{\rho}(1 - \hat{c}) T + \frac{\hat{\rho} h_f}{c_l} \right] \frac{\partial g}{\partial t}$$

$$= \alpha_l \frac{\partial}{\partial x} \left\{ [(1 - g)\hat{k} + g] \frac{\partial T}{\partial x} \right\} \tag{4}$$

$$[g + \beta^j \hat{\rho} \kappa^j (1 - g)] \frac{\partial C_l}{\partial t} + u \frac{\partial C_l}{\partial x} = -\hat{\rho}(1 - \kappa^j) C_l \frac{\partial g}{\partial t} \tag{5}$$

where the superscript j stands for α and β that correspond to the primary solidification and combined regions, respectively. The microsegregation parameter β^j in Eq. (5) represents the degree of back diffusion,[22] by which the interaction between micro- and macrosegregation is incorporated. Settings of $\beta^j = 0$ and 1, respectively, correspond to two limiting cases of solid state diffusion, that is, the Scheil equation and the lever rule. According to assumptions (8) and (9), the microsegregation parameter in each region takes the values of $0 \le \beta^\alpha \le 1$ and $\beta^\beta = 1$.

Because the initial condition is evident, it is omitted here. The boundary conditions at the cooling wall and each of the interfaces can be listed as follows:

$$T = T_W \quad \text{at} \quad x = 0 \tag{6}$$

$$T = T_P \quad \text{at} \quad x = \delta_P \tag{7}$$

$$T = T_L \quad \text{at} \quad x = \delta_L \tag{8}$$

$$T = T_0 \quad \text{as} \quad x \to \infty \tag{9}$$

$$C = C_0 \quad \text{for} \quad x \ge \delta_L \tag{10}$$

$$u^{L-} = u^{L+} = u_l \quad \text{at} \quad x = \delta_L \tag{11}$$

$$\left(k \frac{\partial T}{\partial x} \right)^{L-} - \left(k \frac{\partial T}{\partial x} \right)^{L+} = 0 \quad \text{at} \quad x = \delta_L \tag{12}$$

where the superscripts $L-$ and $L+$ denote the liquidus position approaching from the mush and liquid sides, respectively.

The changes in the physical quantities of interest across the peritectic line play a key role in this analysis. Because of the $\alpha + L \to \beta$ reaction, a finite jump in the liquid fraction occurs at the peritectic line, yielding discontinuities in the velocity, enthalpy, and concentration as well. By applying the conservation principle, we can derive the equations of mass, energy, and concentration for the peritectic line:

$$\left[(\rho_m)^{P+} - (\rho_m)^{P-} \right] \frac{d\delta_P}{dt} = -\rho_l (u^{P+} - u^{P-}) \tag{13}$$

$$\left[(\rho_m h_m)^{P+} - (\rho_m h_m)^{P-} \right] \frac{d\delta_P}{dt}$$

$$= \left(-\rho_l u h_l + k \frac{\partial T}{\partial x} \right)^{P+} - \left(-\rho_l u h_l + k \frac{\partial T}{\partial x} \right)^{P-} \tag{14}$$

$$\left[(\rho_m C_m)^{P+} - (\rho_m C_m)^{P-} \right] \frac{d\delta_P}{dt} = -\rho_l C_l (u^{P+} - u^{P-}) \tag{15}$$

where the superscripts $P-$ and $P+$ denote the peritectic line approaching from the secondary and primary solidification sides, respectively.

The governing equations are similar to those of the binary eutectic system, which were previously presented by Voller[9] and Chung et al.[10] However, the secondary solidification has been newly modeled, and the discontinuity at the peritectic line has been rigorously formulated. The model equations retain convection by shrinkage-induced flow and property variations in the mushy region.

B. Similarity Transformation

The well-known similarity variable $\eta = x/(4\alpha_l t)^{1/2}$ is introduced to transform the governing equations. In the liquid region the temperature profile is already available as[10,11]

$$\frac{T - T_0}{T_L - T_0} = \frac{\operatorname{erfc}(\eta - U_l)}{\operatorname{erfc}(\lambda_L - U_l)} \qquad \text{for} \qquad \lambda_L < \eta < \infty \tag{16}$$

where the transformed interface position $\lambda_L = \delta_L/(4\alpha_l t)^{1/2}$, as well as the liquid velocity $U_l = u_l/(\alpha_l/t)^{1/2}$, is unknown yet. The governing equations, (3–5), which are common to the primary solidification and combined regions, can be transformed into a set of ordinary differential equations as

$$\frac{dU}{d\eta} - (1 - \hat{\rho}) \eta \frac{dg}{d\eta} = 0 \tag{17}$$

$$\frac{d}{d\eta} \left\{ [(1 - g)\hat{k} + g] \frac{dT}{d\eta} \right\} = -2[(1 - g)\hat{\rho}\hat{c} + g] \eta \frac{dT}{d\eta}$$

$$+ 2U \frac{dT}{d\eta} + 2 \left[\hat{\rho}(\hat{c} - 1) T - \frac{\hat{\rho} h_f}{c_l} \right] \eta \frac{dg}{d\eta} \tag{18}$$

$$\hat{\rho}(1 - \kappa^j)\left(T - T_f^j\right) \frac{dg}{d\eta} = \left[\frac{U}{\eta} - g - \beta^j \hat{\rho} \kappa^j (1 - g) \right] \frac{dT}{d\eta} \tag{19}$$

In this procedure the temperature replaces the liquid concentration as a dependent variable of Eq. (19) using the phase equilibrium relation

$$T = T_f^j + m^j C_l \tag{20}$$

Transforming the interfacial conditions at the peritectic line, Eqs. (13–15), along with some manipulations, yields

$$U^{P+} - U^{P-} = \Delta g (\hat{\rho} - 1) \lambda_P \tag{21}$$

$$[\hat{k} + (1 - \hat{k}) g^{P-}] \left(\frac{dT}{d\eta} \right)^{P-} - [\hat{k} + (1 - \hat{k}) g^{P+}] \left(\frac{dT}{d\eta} \right)^{P+}$$

$$= 2\hat{\rho} \Delta g \left[(1 - \hat{c}) T_P + \frac{h_f}{c_l} \right] \lambda_P \tag{22}$$

$$g^{P-} = \frac{(g^{P+} - \kappa^\beta) C_P + (1 - g^{P+}) \left(C_s^\alpha \right)^{P+}}{(1 - \kappa^\beta) C_P} \tag{23}$$

where $\Delta g = g^{P+} - g^{P-}$ and C_s^α denotes the intrinsic volume-averaged concentration of α-phase solid.[25]

The transformed equations, (17–19), are to be solved to obtain $T(\eta)$, $U(\eta)$, and $g(\eta)$. Also the positions of peritectic line δ_P and liquidus δ_L should be determined so as to satisfy the interfacial conditions. Because the inherent complexities stemming from the interface movement pose formidable barriers to closed-form analytic solutions, a numerical approach is invoked to treat the mushy region. In the numerical calculation the primary solidification and combined regions are discretized into 4000 segments for sufficient resolution, respectively. Such a grid system is far beyond the limit of grid independence in this work. The present number is chosen to keep the consistency with the previous semi-analytical works[9–11] in comparative discussion.

Once the temperature field $T(\eta)$ is obtained, the liquid concentration field $C_l(\eta)$ can be determined by Eq. (20). The intrinsic volume-averaged concentration in the β-phase solid C_s^β is readily obtained as $\kappa^\beta C_l$ by the assumption 9. However, because of finite back diffusion in the primary solidification region, the evaluation of the intrinsic volume-averaged concentration in the α-phase solid C_s^α needs a microscopic model. As noted earlier, the Clyne and Kurz model[9,11] is employed in this study:

$$\frac{\mathrm{d}}{\mathrm{d}\eta}\left[(1-g)C_s^\alpha\right] = \frac{\kappa^\alpha}{m^\alpha}\left[\beta^\alpha(1-g)\frac{\mathrm{d}T}{\mathrm{d}\eta} - \left(T - T_f^\alpha\right)\frac{\mathrm{d}g}{\mathrm{d}\eta}\right] \tag{24}$$

Because the mixture concentration characterizes the macrosegregation pattern, it is an important result of the analysis. The solute conservation for mush, along with the predetermined values of C_l, C_s^α, and C_s^β, yields the mixture concentration C_m as

$$C_m = \frac{g\rho_l C_l + (1-g)\rho_s C_s^j}{g\rho_l + (1-g)\rho_s} \qquad (j = \alpha, \beta) \tag{25}$$

C. Interface-Tracking Algorithm

Because the performance of interface tracking essentially affects the overall utility of similarity solutions in the alloy solidification,[9] the development of an efficient routine is no less important than the modeling of physical phenomena. Reviewing the previous works[9–11] leads to the fact that a new algorithm needs to be stable and efficient in convergence regardless of the initially guessed interface positions. In addition, it is desirable that it can be applied to the case of a multicomponent alloy whose solidification path is highly complex.

To determine the liquidus and peritectic line positions, the interfacial energy conditions, Eqs. (12) and (22), are rewritten as follows:

$$F_P(\lambda_P, \lambda_L) = [\hat{k} + (1-\hat{k})g^{P-}]\left(\frac{\mathrm{d}T}{\mathrm{d}\eta}\right)^{P-} - [\hat{k} + (1-\hat{k})g^{P+}] \times \left(\frac{\mathrm{d}T}{\mathrm{d}\eta}\right)^{P+} - 2\hat{\rho}\Delta g\left[(1-\hat{c})T_P + \frac{h_f}{c_l}\right]\lambda_P \tag{26}$$

$$F_L(\lambda_P, \lambda_L) = \left(\frac{\mathrm{d}T}{\mathrm{d}\eta}\right)^{L-} - \left(\frac{\mathrm{d}T}{\mathrm{d}\eta}\right)^{L+} \tag{27}$$

where the transformed positions λ_P and λ_L are to be determined such that the functions F_P and F_L vanish simultaneously. The Newton–Raphson method is invoked to solve the set of nonlinear equations. In the solution procedure we need to evaluate the four tentative temperature gradients designated by the superscripts $L+$, $L-$, $P+$, and $P-$, respectively. The gradients depend on the liquidus and peritectic line positions. The first one, that is, the temperature gradient on the liquid side of the liquidus position, is readily obtained from Eq. (16), but the others are unavailable a priori. As a first approximation, linear temperature profiles in the primary solidification and combined regions are assumed.

$$\left(\frac{\mathrm{d}T}{\mathrm{d}\eta}\right)^{L+} = \frac{2(T_0 - T_L)\exp\left[-(\lambda_L - U_l)^2\right]}{\pi^{\frac{1}{2}}\mathrm{erfc}(\lambda_L - U_l)} \tag{28}$$

$$\left(\frac{\mathrm{d}T}{\mathrm{d}\eta}\right)^{P-} \approx \frac{T_P - T_W}{\lambda_P} \tag{29}$$

$$\left(\frac{\mathrm{d}T}{\mathrm{d}\eta}\right)^{P+} \approx \left(\frac{\mathrm{d}T}{\mathrm{d}\eta}\right)^{L-} \approx \frac{T_L - T_P}{\lambda_L - \lambda_P} \tag{30}$$

Using these values, the two positions are updated as

$$\begin{bmatrix}\lambda_P \\ \lambda_L\end{bmatrix}^n = \begin{bmatrix}\lambda_P \\ \lambda_L\end{bmatrix} - \omega\begin{bmatrix}\dfrac{\partial F_P}{\partial \lambda_P} & \dfrac{\partial F_P}{\partial \lambda_L} \\ \dfrac{\partial F_L}{\partial \lambda_P} & \dfrac{\partial F_L}{\partial \lambda_L}\end{bmatrix}^{-1}\begin{bmatrix}F_P \\ F_L\end{bmatrix} \tag{31}$$

Because the functions F_P and F_L are monotonic with respect to the positions λ_P and λ_L, the preceding algorithm ensures the convergence, and the linear approximation yields the correct direction of change in the updating procedure, Eq. (31). The relaxation factor controls the size of change. In the present analysis the solidus position needs not to be separately tracked because it can be readily obtained from the predetermined liquid fraction field.

To evaluate the performance of the present algorithm, a similarity solution for a typical binary eutectic system is obtained through the same procedure with the previous studies, but using different interface tracking algorithms. Compared with the linearized correction scheme proposed by Chung et al.,[10,11] the present algorithm shows faster convergence (about 30%) and robust stability. In addition, it works well for a wide range of the relaxation factor and is nearly insensitive to the initial guess of the interface positions.

D. Solution Procedure

Summarizing the foregoing analysis, the solution procedure can be specifically itemized as follows:

1) Initially guess the values of λ_P and λ_L.

2) Assume the liquid fraction profile $g(\eta)$ over the whole domain.

3) Calculate the velocity field $U(\eta)$. First, integrate Eq. (17) backward from $\eta = \lambda_L$ to $\eta = \lambda_P$ with the liquid velocity U_l. Next, calculate U^{P-} from the jump condition at the peritectic line, Eq. (21). Finally, integrate Eq. (17) backward from $\eta = \lambda_P$ to $\eta = 0$.

4) Obtain the temperature field $T(\eta)$ by solving Eq. (18) with the boundary conditions, Eqs. (6–8).

5) Obtain the intrinsic volume-averaged concentration of the α-phase solid C_s^α through backward integration of Eq. (24) with $C_{si}^\alpha = \kappa^\alpha C_0$ at the liquidus.

6) Calculate the liquid fraction field $g(\eta)$. First, integrate Eq. (19) backward from $\eta = \lambda_L$ to $\eta = \lambda_P$ with $g^{L-} = 1$ at the liquidus. Next, calculate g^{P-} from the jump condition at the peritectic line, Eq. (23). Finally, integrate Eq. (19) backward from $\eta = \lambda_P$ to $\eta = 0$.

7) Repeat steps 3–6 until the convergence of $T(\eta)$, $U(\eta)$, and $g(\eta)$.

8) Check whether the calculated temperature field satisfies the interfacial conditions, Eqs. (26) and (27), within a prescribed tolerance. If not, update the interface positions using Eq. (31), and then repeat the steps 3–7. On satisfaction, terminate the procedure and calculate the quantities of interest.

In step 2 the liquid fraction profile for the limiting case where convection is absent leads to a more plausible assumption as

$$g(\eta) = \frac{1-g^*}{\lambda_L - \lambda_P}\eta + \frac{g^*\lambda_L - \lambda_P}{\lambda_L - \lambda_P} \qquad \text{for} \qquad \lambda_P < \eta < \lambda_L \tag{32}$$

$$g(\eta) = \frac{g^{**}\eta}{\lambda_P} \qquad \text{for} \qquad 0 < \eta < \lambda_P \tag{33}$$

where g^* and g^{**} are defined as

$$g^* = 1 - \left\lfloor 1 - (C_P/C_0)^{(1-\beta^\alpha\kappa^\alpha)/(\kappa^\alpha - 1)}\right\rfloor \Big/ (1 - \beta^\alpha\kappa^\alpha) \tag{34}$$

$$g^{**} = \lfloor (1-\kappa^\alpha)g^* - (\kappa^\beta - \kappa^\alpha)\rfloor/(1-\kappa^\beta) \tag{35}$$

In step 3 the liquid velocity U_l is evaluated so as to satisfy the overall mass balance:

$$U_l = (1 - \hat{\rho})\lambda_L \left[1 - \frac{1}{\lambda_L} \left(\int_0^{\lambda_P} g \, d\eta + \int_{\lambda_P}^{\lambda_L} g \, d\eta \right) \right] \quad (36)$$

III. Results and Discussion

To obtain specific results, sample calculations for a typical peritectic alloy is carried out. The alloy considered here needs to be chosen carefully because the present model is applicable to the case of nonlayered microstructure. A Pb-Bi binary peritectic system meets the requirement in that it has already been reported to form such a structure and that its properties are well established. The difference between the solid and liquid densities induces a strong interdendritic fluid flow. This shrinkage-induced flow is known to help mixing in the liquid and to destabilize the layer formation, thus leading to the structure of single primary to peritectic phase transition considered here. Numerical data used in the calculations are summarized in Table 1.[26] Remark here that the aim of these sample calculations is to elucidate the capability and utility of our semi-analytical solution, not to investigate the characteristics of peritectic solidification processes.

Although the microstructure of binary hypoperitectic systems is distinct from that of binary eutectic systems, their solidification processes can be modeled in a similar manner, as mentioned earlier. In the case of binary hypoperitectic systems, the unsolidified liquid in mush changes completely to solid at the peritectic temperature (see Fig. 1), yielding a finite jump in the liquid fraction. Because the secondary solidification region is absent, the combined region reduces to a pure solid region. Note that in hyperperitectic systems, the liquid turns only partly into the second phase through peritectic reaction. In binary eutectic systems the interdendritic (or intercellular) liquid entirely solidifies at the eutectic temperature. The two systems show common features: 1) there appear three distinct regions during solidification, that is, liquid, mush, and solid; and 2) a discontinuous change in the liquid fraction occurs at the interface between the mush and solid regions. It is deduced from this discussion that the similarity solution for binary eutectic systems can apply to the case of hypoperitectic systems with minor modifications. This fact provides a basis to validate the present solution.

Two sets of calculation for a hypoperitectic alloy (see Table 1) were performed: one by the present solution and the other by the previous solution.[10] The two results agree indistinguishably with each other, which implies that the present analysis has been based on proper modeling, formulation, and solution procedure. As representative results of the calculation, Figs. 3 and 4 depict the liquid fraction and mixture concentration profiles, respectively, for each of the two back diffusion limits, that is, the Scheil equation and lever rule, in the primary solid phase. It can be confirmed that the effect of back diffusion on the overall solidification process is so significant that it needs to be included in modeling. The finite jump in the liquid fraction at the peritectic line appears clearly in Fig. 3, which is also affected by back diffusion. Macrosegregation is reduced as the microsegregation parameter increases, especially near the peritectic line, which is in line with the case of binary eutectic systems.[10]

Table 1 Numerical data for sample calculations

Property	Value
c	147 J/kgK
k	10 W/mK
ρ_s/ρ_l	10,000/9,900 kg/m^3
h_f	23,000 J/kg
T_P	457 K
T_{f_α}/T_{f_β}	601/563 K
$\kappa^\alpha/\kappa^\beta$	0.6667/0.8045
m^α/m^β	−400/−295 K
T_W	373 K
ΔT	10 K
C_0 hypo/hyper	0.26/0.325 kg/kg

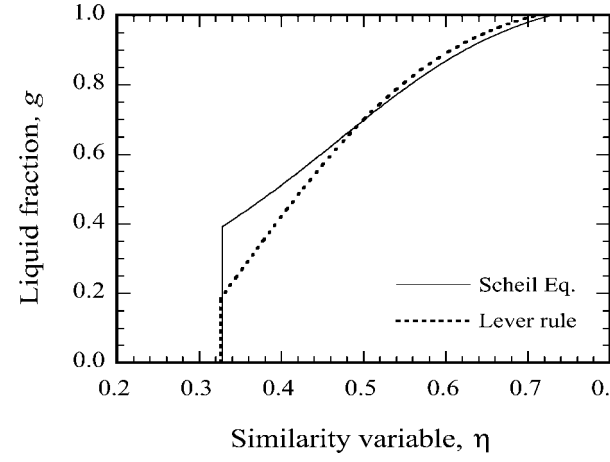

Fig. 3 Liquid fraction profile during solidification of a hypoperitectic alloy for each of two back diffusion limits in the primary phase.

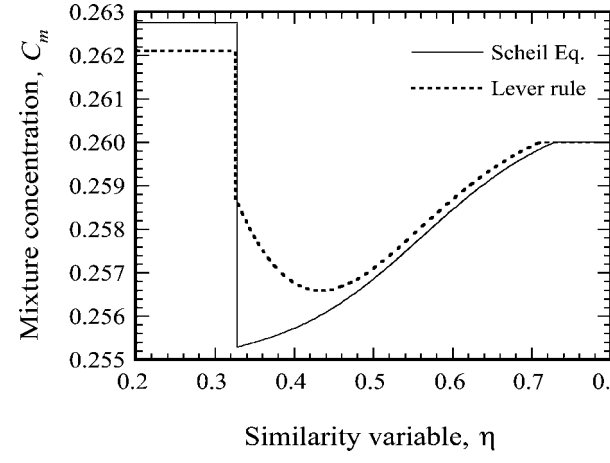

Fig. 4 Mixture concentration profile during solidification of a hypoperitectic alloy for each of two back diffusion limits in the primary phase.

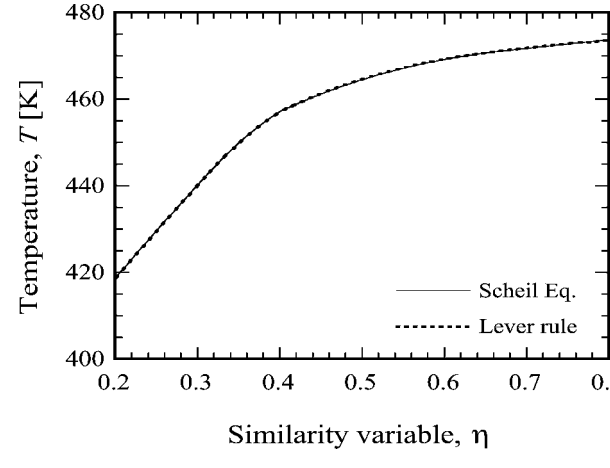

Fig. 5 Temperature profile during solidification of a hyperperitectic alloy for each of two back diffusion limits in the primary phase.

One of the main contributions of this study is to handle hyperperitectic systems semi-analytically, which seems to be the first successful attempt in this area. A sample calculation done for a binary hyperperitectic alloy (see Table 1) might illustrate the capability and utility of the present solution, the results of which are depicted in Figs. 5–9. Both of the two limits of diffusivity are also considered to scrutinize the effect of back diffusion in the primary phase on the overall solidification process. Because peritectic reaction takes place at a constant temperature, the temperature profile (Fig. 5) does not

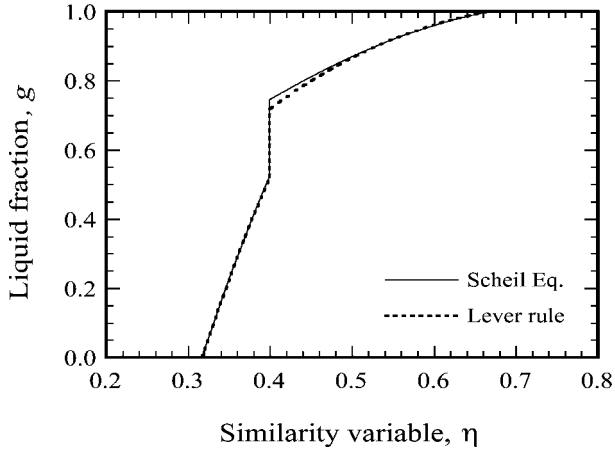

Fig. 6 Liquid fraction profile during solidification of a hyperperitectic alloy for each of two back diffusion limits in the primary phase.

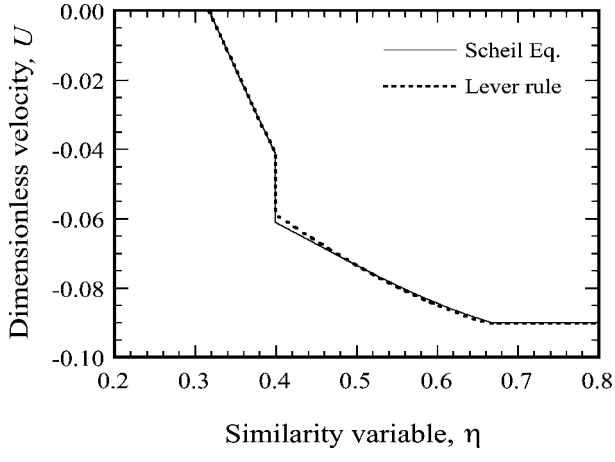

Fig. 7 Velocity profile during solidification of a hyperperitectic alloy for each of two back diffusion limits in the primary phase.

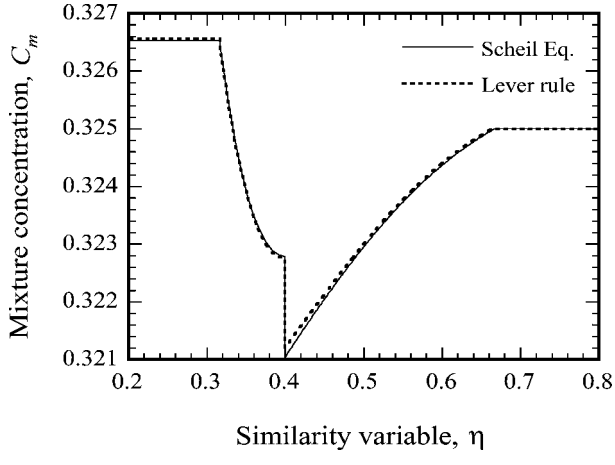

Fig. 8 Mixture concentration profile during solidification of a hyperperitectic alloy for each of two back diffusion limits in the primary phase.

exhibit the characteristic features of peritectic solidification, such as the existence of two mushy regions and discontinuity between them. This is similar to the eutectic line in eutectic systems.[10] However, the features are clearly seen in the liquid fraction profile (Fig. 6), velocity profile (Fig. 7), and mixture concentration profile (Fig. 8). The presence of four distinct regions during peritectic solidification can be identified in the solid concentration profile (Fig. 9). Although the solidus position has not been tracked in the analysis, it can be readily determined by examining the liquid fraction field, that is,

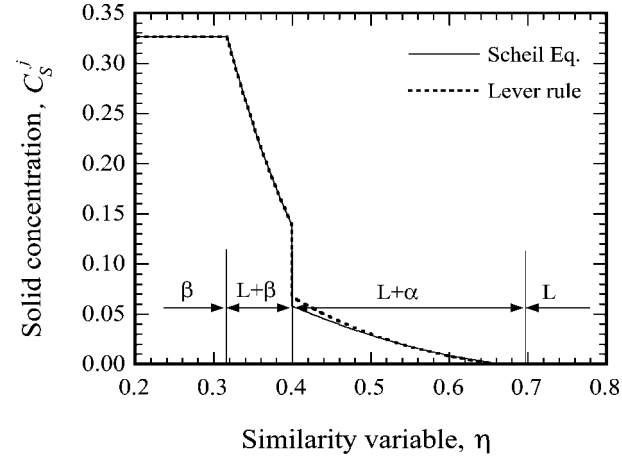

Fig. 9 Solid concentration profile during solidification of a hyperperitectic alloy for each of two back diffusion limits in the primary phase.

$\lambda(g = 0+)$. Based on these results, it is concluded that our solution is capable of resolving most of the characteristic features of peritectic solidification. Considering that the present model already accounted for the essential ingredients of alloy solidification, it is expected that the solution might be useful for validating numerical models as a benchmark.

In addition to the main focus that has just been discussed, some characteristics of peritectic solidification are reported here in association with the already depicted results. The effect of the microsegregation parameter on the macrosegregation pattern in hyperperitectic systems (Fig. 8) is not so clear as in the case of hypoperitectic systems. Although the effect is discernible in the primary solidification region, it nearly disappears in the secondary solidification region. This seems to originate from the following two facts. First, referring to the phase equilibrium diagram (Fig. 1), the primary solidification region of a hyperperitectic alloy is narrower than that of a hypoperitectic one. Thus, the time allowed for back diffusion in the α phase is shorter, yielding relatively small differences in the liquid fraction and concentration between the two diffusivity limits. Second, the present model assumed complete peritectic transformation (assumption 9), that is, all of the α phase formed during the primary solidification turns into the β phase at the peritectic composition. In other words, the concentration of the β-phase solid is always constant regardless of the microsegregation parameter (Fig. 9). Of course, the effect of back diffusion in the primary phase can permeate into the secondary solidification region via the difference in the liquid fraction or the liquid concentration, but it is negligible under the present condition, as already shown in the mixture concentration profile (Fig. 8).

Closing our discussion, it is worth noting the rate of peritectic reaction can have a significant influence on the solute redistribution process during the peritectic solidification. A finite-rate peritectic reaction that seems to occur during the actual solidification process forms the microstructure in which the primary phase is surrounded by the secondary phase. In this case the macrosegregation pattern would differ considerably from the present study employing the complete transformation. A more realistic solution for the directional solidification of peritectic alloys needs further information regarding the rate of peritectic reaction. As noted before, the present approach based on the lever rule in the second solid phase belongs to one of the limiting cases from the viewpoint of peritectic reaction.

IV. Conclusions

A semi-analytical similarity solution for the directional solidification of a binary peritectic alloy in the presence of shrinkage-induced flow has been proposed. In addition to the flow, the present model retains most of the essential ingredients of alloy solidification, such as temperature-solute coupling, macrosegregation, solid–liquid property difference, and finite back diffusion in the primary phase. Based on the Newton–Raphson method and linear approximation of the

temperature profile, a new algorithm for simultaneously tracking the liquidus and peritectic reaction positions has been developed. Sample calculations for both hypo- and hyperperitectic compositions of a typical peritectic alloy have been performed to validate the modeling and to examine the capability and utility of the present solution.

The new tracking algorithm proved to be more efficient and stable in convergence than the existing schemes. In view of its reliable performance, the algorithm can be applied to the analysis of multicomponent alloy systems without additional difficulties. For a hypoperitectic alloy the result by the present solution agrees perfectly with that by a modified version of the existing solution for eutectic systems. The comparison leads to that the present solution has been based on proper modeling, formulation, and solution procedure. A set of representative results for a hyperperitectic alloy successfully resolves the characteristic features of peritectic solidification, such as the existence of two mushy regions and discontinuities in the liquid fraction, velocity, and mixture concentration at their interface. It is concluded from this fact that the present solution can serve as a useful benchmark in the development of numerical models to predict peritectic solidification processes.

References

[1]Boettinger, W. J., Coriell, S. R., Greer, A. L., Karma, A., Kurz, W., Rappaz, M., and Trivedi, R., "Solidification Microstructures: Recent Developments, Future Directions," *Acta Materialia*, Vol. 48, No. 1, 2000, pp. 43–70.

[2]Berkermann, C., and Viskanta, R., "Mathematical Modeling of Transport Phenomena During Alloy Solidification," *Applied Mechanics Reviews*, Vol. 46, No. 1, 1993, pp. 1–27.

[3]Ni, J., and Incropera, F. P., "Extension of the Continuum Model for Transport Phenomena Occurring During Metal Alloy Solidification-II. Microscopic Considerations," *International Journal of Heat and Mass Transfer*, Vol. 38, No. 7, 1995, pp. 1285–1296.

[4]Schneider, M. C., and Beckermann, C., "Formation of Macrosegregation by Multicomponent Thermosolutal Convection During the Solidification of Steel," *Metallurgical and Materials Transactions A*, Vol. 26, No. 9, 1995, pp. 2373–2388.

[5]Swaminathan, C. R., and Voller, V. R., "Toward a General Numerical Scheme for Solidification Systems," *International Journal of Heat and Mass Transfer*, Vol. 40, No. 12, 1997, pp. 2859–2868.

[6]Muehkbauer, J. C., Hatcher, J. D., Lyons, D. W., and Sunderland, J. E., "Transient Heat Transfer Analysis of Alloy Solidification," *Journal of Heat Transfer*, Vol. 95, No. 3, 1973, pp. 324–331.

[7]Worster, M. G., "Solidification of an Alloy from a Cooled Boundary," *Journal of Fluid Mechanics*, Vol. 167, June 1986, pp. 481–501.

[8]Braga, S. L., and Viskanta, R., "Solidification of a Binary Alloy Solution on a Cold Isothermal Surface," *International Journal of Heat and Mass Transfer*, Vol. 33, No. 4, 1990, pp. 745–754.

[9]Voller, V. R., "A Similarity Solution for the Solidification of a Multicomponent Alloy," *International Journal of Heat and Mass Transfer*, Vol. 40, No. 12, 1997, pp. 2869–2877.

[10]Chung, J. D., Lee, J. S., Ro, S. T., and Yoo, H., "An Analytical Approach to the Conduction-Dominated Solidification of Binary Mixtures," *International Journal of Heat and Mass Transfer*, Vol. 42, No. 2, 1999, pp. 373–377.

[11]Chung, J. D., Lee, J. S., Choi, M., and Yoo, H., "A Refined Similarity Solution for the Multicomponent Alloy Solidification," *International Journal of Heat and Mass Transfer*, Vol. 44, No. 13, 2001, pp. 2483–2492.

[12]Kurz, W., and Fisher, D. J., *Fundamentals of Solidification*, Trans Tech Publ., Uetikon-Zurich, 1989, Chap. 5.

[13]Maxwell, I., and Hellawell, A., "An Analysis of the Peritectic Reaction with Particular Reference to Al-Ti Alloys," *Acta Metallurgica*, Vol. 23, Aug. 1975, pp. 901–909.

[14]Goyal, A., Funkenbusch, P. D., Kroger, D. M., and Burns, S. J., "Fabrication of Highly Aligned $Yba_2Cu_3O_{7-\delta}$-Ag Melt-Textured Composites," *Physica C: Superconductivity*, Vol. 182, Nos. 4–6, 1991, pp. 203–218.

[15]Kim, C. J., Kim, K. B., and Hong, G. W., "Influence of Grain Size of $Yba_2Cu_3O_{7-y}$ on the Particle Size of Y_2BaCuO_5 after the Peritectic Reaction," *Materials Letters*, Vol. 21, Sept. 1994, pp. 9–14.

[16]Chen, Z., Wang, N., Song, X., and Wang, X., "Characterization of a New Nd-Fe-O Compound in $Nd_{34}Fe_{60}O_6$ Alloy," *Materials Letters*, Vol. 22, Feb. 1995, pp. 119–123.

[17]Karma, A., Rappel, W. J., Fuh, B. C., and Trivedi, R., "Model of Banding in Diffusive and Convective Regimes During Directional Solidification of Peritectic Systems," *Metallurgical and Materials Transactions A*, Vol. 29A, No. 5, 1998, pp. 1457–1470.

[18]Park, J.-S., and Trivedi, R., "Convection-Induced Novel Oscillating Microstructure Formation in Peritectic Systems," *Journal of Crystal Growth*, Vol. 187, Nos. 3–4, 1998, pp. 511–515.

[19]Boettinger, W. J., "The Structure of Directionally Solidified Two-Phase Sn-Cd Peritectic Alloys," *Metallurgical Transactions*, Vol. 5, Sept. 1974, pp. 2023–2031.

[20]Titchener, A. P., and Spittle, J. A., "The Microstructures of Directionally Solidified Alloys That Undergo a Peritectic Transformation," *Acta Metallurgica*, Vol. 23, April 1975, pp. 497–502.

[21]Ma, D., Li, Y., Ng, S. C., and Jones, H., "Unidirectional Solidification of Zn-rich Zn-Cu Peritectic Alloys—I. Microstructure Selection," *Acta Materialia*, Vol. 48, No. 2, 2000, pp. 419–431.

[22]Clyne, T. W., and Kurz, W., "Solute Redistribution During Solidification with Rapid Solid State Diffusion," *Metallurgical Transactions A*, Vol. 12, June 1981, pp. 965–971.

[23]John, D. H., and Hogan, L. M., "A Simple Prediction of the Rate of the Peritectic Transformation," *Acta Metallurgica.*, Vol. 35, No. 1, 1987, pp. 171–174.

[24]Das, A., Manna, I., and Pabi, S. K., "A Numerical Model of Peritectic Transformation," *Acta Materialia*, Vol. 47, No. 4, 1999, pp. 1379–1388.

[25]Ni, J., and Beckermann, C., "A Volume-Averaged Two-Phase Model for Transport Phenomena During Solidification," *Metallurgical Transactions B*, Vol. 22, June 1991, pp. 349–361.

[26]Touloukian, Y. S., Powell, R. W., Ho, C. Y., and Klemens, P. G., *Thermophysical Properties of Matter*, IFI/Plenum, New York, 1970.